Extended coarse-grained dipole model for polar liquids: Application to bulk and confined water

M. H. Motevaselian, S. Y. Mashayak, and N. R. Aluru[*]

Department of Mechanical Science and Engineering, Beckman Institute for Advanced Science and Technology, University of Illinois at Urbana-Champaign, Urbana, Illinois 61801, USA

We report a multiscale investigation of water inside graphene slitlike channels that extends from the detailed all-atom level (AA) to the cheaper particle-based coarse-grained (CG) level, and to the continuum-based level. Since water is a highly polar solvent, the detailed description of its structural and dielectric properties close to the interfaces is of paramount importance in many applications. For this purpose, we have systematically developed an extended dipole-based CG model using the relative entropy method that can accurately reproduce the radial distribution function (RDF), diffusion coefficient, and bulk dielectric permittivity of the underlying AA reference model. The extended model is simple yet complex enough to shed light on the role of dipolar interactions in polar liquids such as water. Using the CG potentials developed in this work, we show that the structure, parallel dielectric permittivity, and polarization profiles can be captured reasonably well compared to all-atom molecular dynamics simulations. Furthermore, we use the empirical potential-based quasicontinuum (EQT) framework to predict the density and polarization of water molecules inside nanoslit channels of various widths. Our continuum analyses reveal that the mean field treatment of dipolar correlations in combination with the use of CG potentials are sufficient to accurately reproduce the structural variations of water inside the confined graphene slit channels. Finally, by using coarse-grained molecular dynamics and EQT simulations, we comment on the applicability of dipolar-based CG models in reproducing the structure of water near charged interfaces.

I. INTRODUCTION

Water is one of the most abundant molecules on the Earth. Even though it is a chemically "simple" molecule, water has posed a great challenge to the scientific community in terms of describing its behavior at interfaces and in aqueous solutions. Due to its geometry and distinct charge distribution, water is a highly polar molecule with a relatively high dielectric constant. The dielectric permittivity is directly related to the ability of the fluid in screening charges. Thus, the electrostatic interactions of water in the presence of an external field or with charged objects such as charged colloidal particles, ions, proteins, and lipid membranes are profoundly affected by its very existence [1,2]. Thus, an in-depth understanding of these interactions and accurate representation of water screening effects are essential to many applications such as water desalination [3,4], protein folding [5,6], peptides self-assembly [7], double-layer capacitance [8], and electrochemical applications of ionic liquids [9].

Due to its computational cost, many theoretical models treat water as a background solvent with a constant dielectric permittivity [10–13]. Although it is true in the case of bulk water, near interfaces the dielectric permittivity varies significantly. Therefore, considering a uniform permittivity may not accurately reflect the underlying physics of charge screening. In fact, capturing the anisotropic nature of dielectric variations, which are reminiscent of the well-known spatially varying density oscillations at an interface, is of paramount importance to many biological and industrial applications [14,15].

Over the past years, density functional theory (DFT) and high resolution atomistic simulations such as molecular dynamics and Monte Carlo simulations have been adopted to study water for a variety of applications in biology, physics, and material science. From these methods one can obtain molecular insights into the nature of different interactions and interpret the physical phenomena based on the knowledge of statistical mechanics. However, for many practical systems the number of water molecules is of the order of several thousands to millions [16], making these methods forbiddingly expensive to simulate systems involving multiple length scales and timescales ranging from the quantum to atomic to continuum scales. Thus, developing multiscale methods that are accurate, fast, and rooted in statistical mechanics can be of high value.

In order to reduce the computational cost, coarse-grained molecular dynamics (CGMD) simulations can be used to access larger length scales and timescales. The objective of any coarse-grained (CG) simulation is to lower the resolution by representing the system with fewer degrees of freedom, while retaining the necessary details to capture the quantity of interest. For any polar molecule, the dipole-dipole interactions and fluctuations are mainly responsible for the dielectric response of the fluid. These interactions are ubiquitous in nature, and they exist in many systems, such as colloids, ferrorheological and electrorheological fluids [17]. Moreover, in addition to the spherically symmetric short-range interactions, dipolar molecules bring in anisotropic forces due to their

*[*]aluru@illinois.edu

long-range dipole-dipole interactions and, thus, can serve as a simple model to understand the structure, dynamics, and thermodynamic properties of polar fluids or dipolar colloidal systems [17,18].

Recently, there have been efforts to develop CG models that include and optimize charges or dipole moments to reproduce various properties of the reference system. The reason behind such efforts is twofold. First, due to the existence of dipole fluctuations, one can calculate the dielectric constant of the fluid. Since the dielectric permittivity incorporates both short- and long-ranged correlations, it can serve as a good test for the accuracy of an intermolecular potential [19]. On the other hand, the implicit treatment of electrostatic interactions for polar molecules, in particular water, fails to capture their dielectric screening effect [20]. One of the earliest studies is based on the well-known Stockmayer potential [21] (a single-site interaction with an associated orientation), which models water as a hard sphere with a point dipole and is referred to as Bratko, Blum, and Luzar (BBL) model [22]. A soft sticky dipole potential is also developed for liquid water, which is the same as the BBL model, except that the hard-sphere interaction is replaced by the softer Lennard-Jones (LJ) potential [16]. More generally, the generalized Stockmayer (GSM) potential is developed for polar liquids that consists of a spherical kernel with dipole-dipole interaction [23] and has been recently applied for water [24]. There are also efforts to match properties of water to experiments (top-down CG methods). One of the top-down CG approaches that maps water into a single-site CG bead with an embedded point dipole is the electrostatic based (ELBA) model. The model was originally developed for a lipid membrane. The parameters are tuned such that with a loss of local structure, it reproduces the bulk water density, and diffusion at room temperature in a good agreement with experiments [25,26]. In a more systematic way, the force matching technique is used with the Drude-type model, to reproduce the radial distribution functions (RDFs) and the dielectric permittivity of some amines and alcohols such as methanol [27]. In this study, we systematically develop an extended dipole-based model for polar fluids that can accurately predict the radial distribution function (RDF), diffusion coefficient, and the bulk permittivity of the reference all-atom model. We apply our model to reproduce water RDF, diffusion coefficient, and dielectric permittivity in the bulk. For this purpose, we model water molecules into extended dipoles, and optimize the dipole moment within the relative entropy (RE) frame work. However, as we show later in Sec. VI A, the RE minimization alone does not guarantee that the water dipolar properties, in particular the dielectric permittivity, are reproduced by the CG model. Thus, we employ the constrained relative entropy (CRE) method [28] to reproduce the all-atom bulk permittivity in the CG model.

The remainder of the paper is organized as follows. In Sec. II, we provide details on the extended dipole-based CG model and apply it to water molecules. In Sec. III A, we first describe the details of systematic charge optimization within the relative entropy frame work for dipole-based CG models, and then in Sec. III B we describe the CRE method in order to reproduce the bulk water permittivity of an all-atom reference model. In Sec. III C, we discuss how to
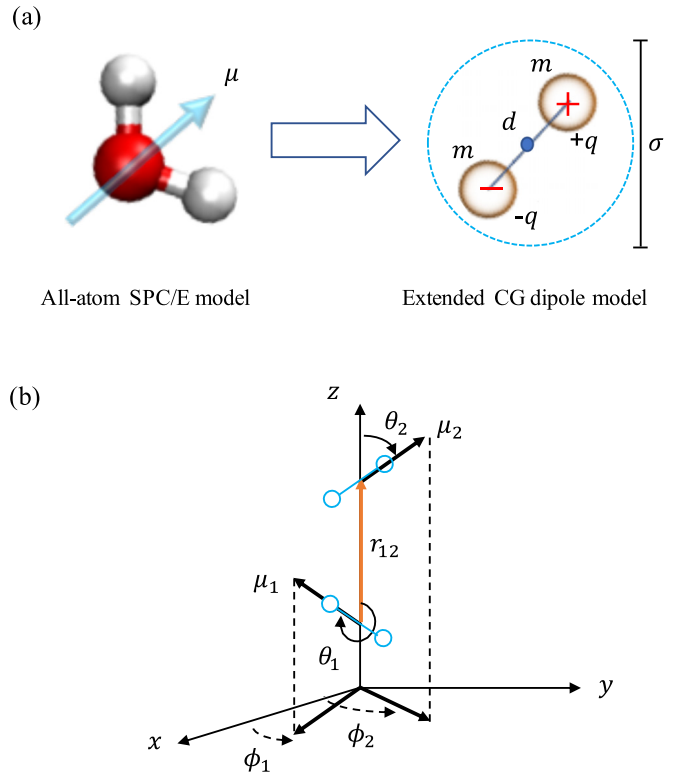

(a)

All-atom SPC/E model   Extended CG dipole model

(b)

FIG. 1. (a) Topology of the extended dipole water molecule. (b) Coordinate system: dipoles are denoted by their dipole vector μ and their corresponding angles (θ, ϕ). r_{12} is the separation distance vector between dipoles μ_1 and μ_2.

match diffusion through modifying the inertia features of our model. In Sec. III D, we discuss systematic coarse graining in inhomogeneous environment by optimizing the wall-fluid interaction energy. In Sec. IV, we describe the theory of the EQT framework. In Sec. V, necessary details of the MD, CG, and EQT simulations are provided. In Sec. VI, we first provide the CG potentials obtained via charge and dielectric permittivity optimization. We then demonstrate the ability of our CG models in reproducing density and parallel permittivity profiles of water molecules inside neutral graphene channels of various widths. In addition, using the empirical potential-based quasicontinuum (EQT) framework, we investigate the applicability of the mean field approximation (MFA) for capturing the dipolar interactions inside the slitlike graphene channels. Finally, we draw conclusions in Sec. VII.

II. CG EXTENDED DIPOLE MODEL

In this study, we consider a CG model consisting of extended dipolar molecules [29,30], in which two opposite charges, $\pm q$, are located at a distance d from each other, thereby creating a dipole moment of $\mu = qd$. The topology of the extended dipole molecule is shown in Fig. 1(a). It can be seen that the molecule has an effective diameter of σ and a van der Waals (vdW) interaction site that is located at the center, $d/2$ distance away from either of the charges. Thus, the interaction energy between the extended dipolar molecules consists of four Coulombic interactions due to

the positive and negative charges, and a vdW pair potential between the molecules center. Compared to the point dipole spherical models, the extended dipole model provides a more realistic picture of highly polar fluids [29]. In addition, it has been shown that for $d/\sigma \leqslant 0.25$, the extended dipole and point dipole models are similar. In this study, we assumed that the distance d is fixed, so the CG model is not polarizable. Although the distance between the charges can be considered as an optimization parameter, for simplicity we only consider optimizing the charges on the molecule as well as the vdW interaction. In order to optimize the charges and the vdW interaction, we follow a systematic bottom-up coarse-graining approach to reproduce the properties of the underlying all-atom (AA) reference model. To demonstrate our model, we coarse grain the all-atom SPC/E water into the extended dipolar molecules with $d = 0.058$ nm, which represents the distance between the oxygen and the center of the line intersecting the hydrogen atoms in the SPC/E AA water model.

III. CG OPTIMIZATION

Our objective is to reproduce the RDF, diffusion coefficient, and the dielectric permittivity in the bulk CG system. There are various systematic CG methods such as iterative Boltzmann inversion (IBI) [31], inverse Monte Carlo (IMC) [32], and RE minimization [33,34] that can accurately reproduce the AA target RDFs. When RDF is the only target of interest, the choice of center-of-mass (COM) mapping of atoms or molecules into spherical beads is a common choice. However, to reproduce the dielectric permittivity, one needs to take into account the dipolar fluctuations. So, for a CG system to be able to predict the dielectric constant, dipole-dipole interactions have to be explicitly considered in the model.

In this study, we use the RE framework to systematically optimize the vdW and electrostatic interactions between the extended dipolar molecules to reproduce the RDF and dielectric constant of the SPC/E water at the temperature of 298 K and density of 1.0 g/cm³.

A. Charge optimization

Relative entropy quantifies to what extent the configurational probability distributions vary from one another between the CG and AA models. Therefore, minimizing the relative entropy with respect to the potential parameters results in the CG energy landscape that reproduces as best as possible the underlying AA probability distribution function in the CG degrees of freedom. It has been shown that in the canonical ensemble the RE can be written as [33]

$$S_{\text{rel}} = \beta\langle U_{\text{CG}} - U_{\text{AA}}\rangle_{\text{AA}} - \beta(F_{\text{CG}} - F_{\text{AA}}) + \langle S_{\text{map}}\rangle_{\text{AA}}, \quad (1)$$

where U is the total energy, F is the configurational part of the Helmholtz free energy, $\langle \ldots \rangle$ represents the Boltzmann weighted average in the corresponding ensemble, S_{map} is the mapping degeneracy in the AA model, and $\beta = 1/k_B T$ with k_B as the Boltzmann constant and T as the temperature. As mentioned earlier, the interaction energy for a system of the extended dipolar molecules consists of the vdW and Coulombic part. We assume that the total CG interaction

energy is pairwise additive, and we model it as

$$U_{\text{CG}} = \sum_{i=1}^{N} \sum_{j>i}^{N} u_{\text{dd,CG}}(r_{ij}), \quad (2)$$

where the summations are over all the distinct dipole molecules, N is the number of dipolar molecules, r_{ij} is the center-to-center distance between i and j dipoles, and $u_{\text{dd,CG}}$ is the CG pair potential between two extended dipole molecules, which is defined as

$$u_{\text{dd,CG}}(r_{ij}) = u_{\text{vdW,CG}}^{\text{ff}}(r_{ij}) + u_{\text{elec,CG}}^{\text{ff}}(r_{ij}), \quad (3)$$

where $u_{\text{vdW,CG}}^{\text{ff}}$ is the coarse-grained fluid-fluid vdW potential and $u_{\text{elec,CG}}^{\text{ff}}$ represents the fluid-fluid electrostatic interaction between two extended dipole molecules. In order to determine the $u_{\text{vdW,CG}}^{\text{ff}}$ in Eq. (3), we model it by uniform cubic-B splines, due to their flexibility and robustness. Hence, $u_{\text{vdW,CG}}^{\text{ff}}$ can be expressed as

$$u_{\text{vdW,CG}}^{\text{ff}}(r) = [1 \quad t \quad t^2 \quad t^3]\frac{1}{6}$$
$$\times \begin{bmatrix} 1 & 4 & 1 & 0 \\ -3 & 0 & 3 & 0 \\ 3 & -6 & 3 & 0 \\ -1 & 3 & -3 & 1 \end{bmatrix} \begin{bmatrix} c_j \\ c_{j+1} \\ c_{j+2} \\ c_{j+3} \end{bmatrix}, \quad (4)$$

where the separation interval from 0 to the cutoff, $R_{\text{cut}}^{\text{ff}}$, is discretized into $n - 1$ segments $\{r_0, r_1, r_2, \ldots, r_{n-1}\}$, of equal size $\Delta r = R_{\text{cut}}^{\text{ff}}/(n - 1)$ such that $r_i = i \times \Delta r$ [$i \in (0 \ldots n - 1)$], $\{c_0, c_1, c_2, \ldots, c_{n+1}\}$ are the spline knots, the index j satisfies the condition $r_j \leqslant r < r_{j+1}$, and $t = \frac{r-r_j}{\Delta r}$. According to Fig. 1(a), the electrostatic part of the pair potential in Eq. (3) can be written as

$$u_{\text{elec,CG}}^{\text{ff}}(r_{ij}) = A_c \sum_{l=1}^{2} \sum_{k=1}^{2} \frac{q_{il}q_{jk}}{4\pi \varepsilon_0 |\mathbf{r}_{il} - \mathbf{r}_{jk}|}, \quad (5)$$

where q_{il} and q_{jk} are the point charges of dipole molecules i and j, respectively, $q_{i1} = q_{j1} = -q$ and $q_{i2} = q_{j2} = +q$, in which q is set to the charge of the oxygen atom in the SPC/E water model, i.e., $q = 0.8476$, ε_0 is the vacuum dielectric permittivity, and $\mathbf{r}_{il}$ and $\mathbf{r}_{jk}$ are the positions of q_{il} and q_{jk}, respectively. In Eq. (5), A_c is the charge scalar factor to be optimized within the relative entropy framework.

Given the definitions of the pair potentials in Eqs. (4) and (5), the optimization parameters consist of a set of knot values and a scalar charge factor, i.e., $\boldsymbol{\lambda} = \{c_0, c_1, \ldots, c_{n+1}, A_c\}$. Since all the adjustable parameters are linear coefficients in the potential, there exists a single global minimum for the relative entropy function [34]. To obtain these parameters, we use the Newton-Raphson optimization technique. In each iteration, the parameters are obtained from the following relation:

$$\boldsymbol{\lambda}^{(k+1)} = \boldsymbol{\lambda}^{(k)} + \omega \, d\boldsymbol{\lambda}, \quad (6)$$

where ω is the relaxation factor and $d\boldsymbol{\lambda}$ is the change in the parameters at each iteration, and is given by

$$d\boldsymbol{\lambda} = -\boldsymbol{H}_{S_{\text{rel}}}^{-1} \cdot \nabla_{\boldsymbol{\lambda}} S_{\text{rel}}, \quad (7)$$

where $\boldsymbol{H}_{S_{\text{rel}}}$ is the Hessian matrix. For more information regarding the expressions in Eq. (7) as well as the implementation, see Ref. [35].

Although optimizing the CG pair potential ($u_{\text{vdW,CG}}^{\text{ff}}$) indirectly affects the dipolar orientations due to the change in the molecular packing, the electrostatic interaction plays an influential role on the dipole-dipole distribution, thereby directly affecting the dielectric permittivity of the fluid. In this study, we optimize the electrostatic interaction through the scalar charge factor A_c. To gain more insight into what optimizing the parameter A_c means, we take a look at the first derivative of the relative entropy. To minimize the RE function, the optimality condition requires that the first derivative of S_{rel} with respect to any parameter be zero, i.e.,

$$\frac{\partial S_{\text{rel}}}{\partial \lambda} = \beta \left(\left\langle \frac{\partial U_{\text{CG}}}{\partial \lambda} \right\rangle_{\text{AA}} - \left\langle \frac{\partial U_{\text{CG}}}{\partial \lambda} \right\rangle_{\text{CG}} \right) = 0. \quad (8)$$

Thus, by using Eqs. (2) and (8), and choosing λ to be A_c, we arrive at

$$\left\langle \sum_{i,j=1,j>i}^{N} \sum_{l,m=1}^{2} \frac{q_{il}q_{jm}}{4\pi\varepsilon_0 r_{ij}} \right\rangle_{\text{AA}} = \left\langle \sum_{i,j=1,j>i}^{N} \frac{u_{\text{elec,CG}}^{\text{ff}}(r_{ij})}{A_c} \right\rangle_{\text{CG}}. \quad (9)$$

The right-hand side of Eq. (9) is equal to the average CG electrostatic potential divided by the factor A_c. Thus, by optimizing A_c, one can obtain the full average electrostatic potential (both short and long range) energy in the mapped all-atom ensemble. In other words,

$$\left\langle U_{\text{elec,AA}}^{\text{dd}} \right\rangle = \frac{1}{A_c} \langle U_{\text{elec,CG}} \rangle, \quad (10)$$

where $U_{\text{elec,CG}}$ is the total electrostatic potential energy of the CG system and $U_{\text{elec,AA}}^{\text{dd}}$ represents the dipolar part of electrostatic potential in the all-atom reference simulation.

B. Dielectric permittivity optimization

For a homogeneous system (bulk) of polar molecules with periodic boundary conditions, the bulk dielectric permittivity is related to the fluctuation of the dipole moment and can be calculated from the following relation [36,37]:

$$\varepsilon_r = 1 + \frac{\langle \boldsymbol{M}^2 \rangle}{3\varepsilon_0 V k_B T}, \quad (11)$$

where ε_r is the bulk dielectric permittivity, V is the volume of the system, and $\boldsymbol{M}$ is the total dipole moment of the liquid defined as

$$\boldsymbol{M} = \sum_{i=1}^{N} \boldsymbol{\mu}_i. \quad (12)$$

Certainly, scaling the charges through parameter A_c affects the value of the dielectric permittivity. However, for a highly polar molecule such as water, where hydrogen bonding plays an important role, the RE minimization alone does not guarantee that the bulk dielectric permittivity is reproduced. Hence, to reproduce ε_r for water, we enforce it as a constraint in the RE minimization. For this purpose, we use the constraint

relative entropy minimization method proposed in Ref. [28]. In general, the CRE has the form

$$S_{\text{crel}} = S_{\text{rel}} + \chi C(\lambda), \quad (13)$$

where χ is the Lagrange multiplier, and $C(\lambda)$ is the imposed constraint. To obtain the optimal parameters, we use Eq. (6) with $d\lambda$ replaced by $d\lambda^c$, which is given by

$$d\lambda^c = d\lambda + \boldsymbol{H}_{S_{\text{rel}}}^{-1} \boldsymbol{J}^T \cdot \left(\boldsymbol{J} \cdot \boldsymbol{H}_{S_{\text{rel}}}^{-1} \boldsymbol{J}^T \right)^{-1} [C(\lambda) + \boldsymbol{J} \cdot d\lambda], \quad (14)$$

where $\boldsymbol{J}$ is the constraint Jacobian matrix. For the detailed derivation of the CRE method, see the Supplemental Material of Ref. [28]. In this study, we define C as

$$C = \frac{1}{2} \left(\frac{\varepsilon_{r,\text{CG}} - \varepsilon_{r,\text{AA}}}{\varepsilon_{r,\text{AA}}} \right)^2, \quad (15)$$

and the corresponding Jacobian matrix has only a nonzero value with respect to the parameter A_c. Thus, it can be written as

$$J = \left(\frac{\varepsilon_{r,\text{CG}} - \varepsilon_{r,\text{AA}}}{\varepsilon_{r,\text{AA}}} \right) \frac{d\varepsilon_{r,\text{CG}}}{dA_c}, \quad (16)$$

where the first derivative of ε_r with respect to A_c can be written as

$$\frac{d\varepsilon_{r,\text{CG}}}{dA_c} = \frac{\varepsilon_{r,\text{CG}} - 1}{A_c}. \quad (17)$$

For details on the derivation of Eq. (17), see Appendix.

C. Matching diffusion coefficient

In this study, we have also examined the diffusion coefficient of the extended dipole model. As it is the case for any CG model, the consequence of removing degrees of freedom is lower friction which results in faster dynamics for the CG models compared to the all-atom counterparts. Thus, the diffusion coefficient obtained from the CGMD simulations is typically an order of magnitude higher than the AAMD simulations [38]. One way to match the diffusion coefficient is to modify the equations of motion via a thermostat that alters the viscous frictional forces on the particles [39]. The other way is to modulate the diffusion coefficient through particles' inertia features [25]. Since the distance within the extended dipole molecule is fixed, we optimize the moment of inertia via changing the mass of the molecule. To match the diffusion coefficient, we used the downhill simplex algorithm with the following objective (or penalty) function:

$$y = |D_{\text{tgt}} - D_{\text{CG}}|, \quad (18)$$

where D_{tgt} and D_{CG} are the diffusion coefficients of the AA reference and CG simulations, respectively, which can be calculated from the Einstein relation

$$D = \lim_{t \to \infty} \frac{1}{6tN} \sum_{i=1}^{N} \langle [\boldsymbol{r}_i(t) - \boldsymbol{r}_i(0)]^2 \rangle. \quad (19)$$

D. Wall-fluid potential for confinement

It is known that the bottom-up systematic CG potentials developed for bulk systems may not be transferable in the

presence of an external potential. For instance, it has been shown that the bulk-based CG potential may not adequately represent the water structure close to the planar graphene sheets [40]. Recently, there have been efforts to develop systematic ways of coarse graining for inhomogeneous systems. Mashayak and Aluru [41] employed the RE method to coarse grain both fluid-fluid and wall-fluid interactions inside the slitlike graphene channels. They have shown that by coarse graining the wall-fluid interaction, the water density profile can be predicted reasonably well when compared to the reference AA simulations. Sanyal and Shell [42] have developed a local density-based approach that modifies the fluid-fluid interactions through a local density potential function. Wagner *et al.* [43] proposed an order-parameter dependent potential, in which they have used the multiscale coarse-graining (MS-CG) approach [44,45] where the order parameter can be local, such as local density at a CG site, or global, such as the distance from a wall. In this study, we use the approach of Mashayak *et al.* [41], except that we use the bulk-based CG pair potential for the fluid-fluid interaction and optimize the wall-fluid interaction within the RE framework. Thus, compared to Eq. (2) the total potential of a confined CG system will have an additional contribution from the wall that depends on the separation distance between the wall and the fluid, and it can be written as

$$U_{CG}^{wf} = \sum_{i=1}^{N_w} \sum_{j=1}^{N_f} u_{CG}^{wf}(r_{ij}), \qquad (20)$$

where N_w and N_f are the number of wall atoms and confined fluid atoms, respectively, and u_{CG}^{wf} is the CG wall-fluid pair potential that is optimized to account for the missing structure nearby the wall-fluid interface. Similar to the bulk fluid-fluid potential $u_{vdW,CG}^{ff}$, we use Eq. (4) to model the wall-fluid pair interaction in our simulations. Therefore, for the confined system of extended dipole molecules we perform an additional optimization to determine the CG wall-fluid interaction.

IV. EQT

EQT is an empirical potential-based quasicontinuum theory that seamlessly integrates the atomistic pair potentials into a continuum framework such as the Nernst-Planck (NP) equation. For a slit channel with the z axis as the inhomogeneous direction, the one-dimensional (1D) steady-state NP equation can be written as

$$\frac{d}{dz}\left(\frac{d\rho(z)}{dz} + \frac{\rho(z)}{k_B T}\frac{dU(z)}{dz}\right) = 0, \qquad (21)$$

with boundary conditions

$$\rho(0) = 0, \qquad (22a)$$

$$\rho(H) = 0, \qquad (22b)$$

$$\frac{1}{H}\int_0^H \rho(z)\,dz = \rho_{avg}, \qquad (22c)$$

where $\rho(z)$ and $U(z)$ are the density and total potential of the molecule at location z, respectively, H is the channel width, and ρ_{avg} is the average density inside the channel.

In the past few years, EQT has been shown to accurately predict the structure and potential of mean force profiles for confined LJ fluids [46,47], CO_2 [48], water [40,41], and electrolytes [30,49]. It has also been used within the classical density functional theory (cDFT) to predict various thermodynamic properties of confined LJ fluids and their mixtures [50–52]. As shown in [51,52], upon minimizing the grand potential of a confined fluid in contact with a bulk reservoir, the equilibrium density profile satisfies the Boltzmann relation

$$\rho(\mathbf{r}) = \rho_b \exp\left[-\frac{1}{k_B T}\left(U^{wf}(\mathbf{r}) + \frac{\delta F^{ex}[\rho(\mathbf{r})]}{\delta\rho(\mathbf{r})} - U_b\right)\right], \qquad (23)$$

where ρ_b and U_b are the density and potential energy in the bulk, respectively, U^{wf} is the total wall-fluid potential, and F^{ex} is the excess part of the intrinsic Helmholtz free energy that contains all the information about the fluid-fluid interaction. We note that the solution of Eqs. (21) and (22) is equivalent to Eq. (23), when the reference point is chosen in the bulk. For a neutral wall, the total wall-fluid potential is written as

$$U^{wf}(\mathbf{r}) = \int \rho_w(\mathbf{r}')u^{wf}(r)d\mathbf{r}', \qquad (24)$$

where $r = |\mathbf{r} - \mathbf{r}'|$, ρ_w is the wall density, and $u^{wf}(r)$ is the effective pair potential between the wall atom and the fluid molecule. For a simple LJ fluid, the wall-fluid pair potential is taken from the reference all-atom simulations, whereas in a system for which the wall-fluid interaction is coarse grained, the wall-fluid potential is taken from the CG system, i.e., $u^{wf}(r) = u_{CG}^{wf}(r)$. In this way, we systematically incorporate the information at the finer level into the continuum representation. The excess free energy functional is split into hard sphere and dispersion parts as

$$F^{ex}[\rho(\mathbf{r})] = F_{hs}^{ex}[\rho(\mathbf{r})] + F_{disp}^{ex}[\rho(\mathbf{r})]. \qquad (25)$$

We note that this is similar to what Mashayak *et al.* have used in the Langevin-Poisson-EQT method [30]. The first term in Eq. (25) is due to the hard sphere repulsion, which is calculated in the fundamental measure theory (FMT) using [53–57]

$$F_{hs}^{ex}[\rho(\mathbf{r})] = k_B T \int \Phi[n_\alpha(\mathbf{r})]d\mathbf{r}, \qquad (26)$$

where Φ is the reduced free energy density, and n_α are the set of weighted densities that come in the scalar and the vector forms, and are defined as

$$n_\alpha(\mathbf{r}) = \int d\mathbf{r}'\rho(\mathbf{r}')\omega_\alpha(\mathbf{r} - \mathbf{r}'). \qquad (27)$$

In Eq. (27), ω_α are the weight functions that are related to the geometrical measures (center of mass, surface area, and volume) of a spherical particle of radius R_{hs}. The detailed implementation of the above functionals and the weight functions in a slit channel are given in the Appendix of Ref. [30].

The second term in Eq. (25) is the excess free energy functional that accounts for the fluid-fluid dispersion interactions. Using the mean field approximation (MFA), F_{disp}^{ex} can be modeled as

$$F_{disp}^{ex}[\rho(\mathbf{r})] = \int\int \rho(\mathbf{r})\rho(\mathbf{r}')u^{ff}(r)d\mathbf{r}\,d\mathbf{r}', \qquad (28)$$

where $u^{\text{ff}}(r)$ is the effective fluid-fluid potential, and r is bounded between the inner and outer cutoffs, R_{min} and R_{cut}, respectively. Similar to the treatment of the wall-fluid potential, the effective fluid-fluid interaction is taken from the CG model, i.e., $u^{\text{ff}}(r) = u^{\text{ff}}_{\text{vdW,CG}}(r)$. We note that due to the mean field approximation and absence of an external electric field, all the dipole orientations are equally likely [58]. Hence, there would be no electrostatic contribution to the excess free energy functional [Eq. (25)].

Once the excess free energy functional is determined, using Eqs. (25), (26), and (28), Eq. (23) can be rewritten as

$$\rho(\mathbf{r}) = \rho_{\text{b}} \exp\left(-\frac{1}{k_B T}\left[U^{\text{wf}}(\mathbf{r}) + U^{\text{ff}}_{\text{hs}}(\mathbf{r}) + U^{\text{ff}}_{\text{CG}}(\mathbf{r}) - U_{\text{b}}\right]\right),$$
(29)

where $U^{\text{ff}}_{\text{hs}}$ is obtained by taking functional derivative of $F^{\text{ex}}_{\text{hs}}$ [Eq. (26)]:

$$U^{\text{ff}}_{\text{hs}}(\mathbf{r}) = k_B T \int d\mathbf{r}' \frac{\partial \Phi(\{n_\alpha\})}{\partial n_\alpha} \frac{\delta n_\alpha(\mathbf{r}')}{\delta \rho(\mathbf{r})},$$
(30)

and the CG fluid-fluid potential energy is given by

$$U^{\text{ff}}_{\text{CG}}(\mathbf{r}) = \int_{r=R_{\text{min}}}^{r=R_{\text{cut}}} \rho(\mathbf{r}') u^{\text{ff}}_{\text{vdW,CG}}(r) d\mathbf{r}'.$$
(31)

V. SIMULATION DETAILS

A. MD simulations

In general, for any bottom-up coarse-graining method, a set of reference trajectories are required to obtain the corresponding CG potentials. As mentioned in Sec. II, we parametrized the CG potentials to reproduce RDF and dielectric constant of the bulk SPC/E water. All the simulations were performed in the canonical ensemble (NVT) using the GROMACS [59] software. Equations of motion are integrated with the leap-frog algorithm with a time step of 1 fs. During the simulations the temperature is kept constant at 298 K using the Nosé-Hoover thermostat [60] with a 0.2 ps time constant. For the bulk simulations, all systems were initially equilibrated for 2 ns, following 10 ns of production run. The SHAKE algorithm [61] was used to keep water molecules rigid. For the short-ranged interactions, the cutoff radius was set to 1.2 nm. Both energy and pressure tail corrections [62] have been applied to the standard 12-6 LJ potential for the bulk MD simulations. The long-range electrostatic interactions were calculated using the particle mesh Ewald (PME) summation [63] with the tinfoil boundary condition (infinite dielectric) and a fast Fourier transform (FFT) grid spacing of 0.12 nm. Periodic boundary conditions were applied in all the directions. In order to obtain enough statistics to calculate the bulk dielectric permittivity, trajectories of atoms were collected every 0.1 ps. For the confined water simulations, our system consists of two parallel graphene sheets separated at a distance of H in the z direction. The lateral dimensions lie in the xy plane with an area of 3.834×3.68927 nm². A periodic boundary condition was applied in all the directions with an extra vacuum of 30σ (where σ is the diameter of the water oxygen atom, and is equal to 0.317 nm) in the z direction to avoid slab-slab interactions between periodic images.

The LJ length and energy scale parameters for carbon-water interaction (σ_{cw}, ε_{cw}) are 0.327 77 nm and 0.389 59 kJ/mol, respectively. The cutoff radius for the short-ranged interactions was set to 0.9 nm. During the simulation, the graphene sheets were frozen, i.e., their positions were not updated. In this study, we have considered simulating water in neutral channels of width 10σ, 7σ, and 4σ. The number of water molecules in these channels and the interaction parameters are adopted from [40]. Additionally, we have simulated water in a capacitor channel of width 12σ, where a uniform partial charge was assigned to the wall atoms to achieve the surface charge density of -0.061 C/m² and $+0.061$ C/m² for the left ($z = 0$) and right ($z = H$) walls, respectively. The number of water molecules inside the channel were tuned such that the water bulk density is recovered in the middle of the channel. In order to obtain reliable results, especially in calculating the dielectric permittivity, the equilibrium properties are averaged over a set of 7 MD simulations of length 8 ns, in which the first 2 ns were discarded.

B. CG simulations

For all the CGMD simulations, we follow the same procedure as in AAMD simulations (see Sec. V A). To obtain the CG potentials and parameters, we used and modified the VOTCA software [35] to perform RE and CRE minimization. To obtain the CG potentials, PME is used for long-ranged electrostatic interactions. Nevertheless, we have also examined using the reaction field to incorporate the water screening effects through a constant dielectric permittivity of 71.89, in accordance with the SPC/E water model dielectric constant. The cutoff used for the short-ranged Coulomb interactions with reaction field was chosen based on the correlation length of the dipole-dipole pair correlation function, which is chosen as 1.2 nm. Beyond this distance, the dipole-dipole pair correlation function decays to zero. Therefore, based on this criterion we treat water as a continuum dielectric media beyond 1.2 nm. Furthermore, to verify 1.2 nm is an appropriate cutoff for the reaction field, we performed another simulation with a cutoff of 1.5 nm and found no changes in the results. Once the optimal CG potentials are obtained, we perform the downhill simplex algorithm implemented in VOTCA package [35] to reproduce the diffusion coefficient of SPC/E water at the temperature of 298 K and density of 1.0 g/cm³. We verified that the water structure, permittivity, and all the correlation functions remained unchanged upon matching diffusion or using reaction field for electrostatic interactions. Finally, with the aid of the softer CG potentials, we can increase the integration time step to speed up and run longer simulations. For this purpose, we setup the CGMD simualtion with the time step of 6 fs, and we observed that the results were unchanged. Therefore, on four cores of Intel Xenon CPU ES-1607 3.00GHz processor compared to the AAMD simualtions, the CGqε model is about an order of magnitude faster. In addition, using the reaction field instead of PME gives an extra speedup factor of $\sim$1.5 in the CGMD simulations. The potential parameters and tables along with the running files for CGMD simulations are publicly available on GITHUB [64].

C. EQT simulations

To obtain density and potential profiles in the EQT simulations, we self-consistently solve Eqs. (24) and (29)–(31). To obtain the bulk potential in Eq. (29), we use Eqs. (30) and (31) with the corresponding bulk density. For all the pair interactions the cutoff radius is set to 0.9 nm consistent with the confined AAMD and CGMD simulations. The R_{min}^{ff} and the hard sphere diameter d_{hs} are set to 0.26 and 0.27 nm, respectively. These values are chosen such that the density profiles from the EQT simulations compare well with the AAMD simulations. As mentioned in Sec. IV all the vdW pair interactions are adopted from the CGMD simulations. By incorporating the interaction information at a finer level, EQT bridges the gap between the atomistic and the continuum representations. In EQT, we approximate the wall by a continuum media with a uniform density. In the case of a graphene interface, the wall density ρ_{wall} is set to 38.18 atoms/nm^3. Given the set of parameters and potentials, we start with the bulk density as our initial guess and iteratively solve the aforementioned equations using the Picard iteration method with a relaxation factor of 0.02.

In order to obtain the density, orientation, and polarization profiles for the capacitor wall, EQT is coupled with the Poisson equation to account for the electrostatic interactions between the wall and dipoles through the mean field approximation and the Langevin dipole (LD) model [30]. Unlike the neutral wall case, oppositely charged walls generate an external electric field that directly affects the molecule dipole orientation. In this case, in addition to the vdW interactions, the total potential energy has a nonzero electrostatic part which can be written as

$$U_{elec}(z) = \mu \langle \cos\theta(z)\rangle \frac{d\phi(z)}{dz}, \tag{32}$$

where ϕ is the electrostatic potential, $\cos\theta(z)$ is the average cosine of dipole orientation, and θ is defined as an angle between the positive z axis and the dipole moment vector. In Eq. (32), the electrostatic potential can be obtained from the Poisson equation. For the case of ion-free water confined in a capacitor wall, the Poisson equation reads as

$$\frac{d^2\phi}{dz^2} = \frac{1}{\epsilon_0}\frac{dP_\perp(z)}{dz}, \tag{33}$$

with the following boundary conditions:

$$\left.\frac{d\phi}{dz}\right|_{z=0} = -\frac{\sigma_{wall\text{-}L}}{\varepsilon_0}, \tag{34a}$$

$$\left.\frac{d\phi}{dz}\right|_{z=H} = \frac{\sigma_{wall\text{-}R}}{\varepsilon_0}, \tag{34b}$$

$$\phi(z = H/2) = 0, \tag{34c}$$

where $\sigma_{wall\text{-}L}$ and $\sigma_{wall\text{-}R}$ are the surface charge densities of the left ($z = 0$) and right ($z = H$) walls, respectively. Furthermore, in Eq. (33), $P_\perp(z)$ is the perpendicular orientation polarization which can be expressed as

$$P_\perp(z) = \rho(z)\mu\langle\cos\theta(z)\rangle. \tag{35}$$

In order to avoid the divergence of Picard iteration, we start with the neutral wall solution (density) and increase the
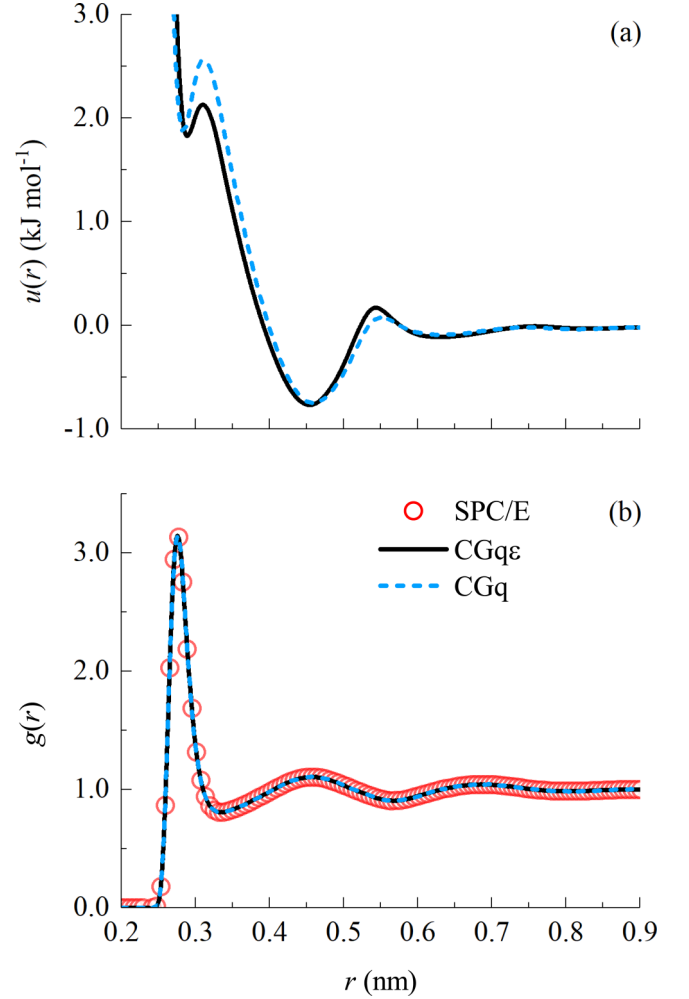

FIG. 2. (a) Dipole-dipole CG potentials obtained by CGq and CGqε methods. (b) Comparison of the center-of-mass radial distribution functions from AAMD and CGMD simulations.

surface charge density in a step by step manner using an increment of 0.0122 C/m^2. In each step, we determine the density profile and use it as an initial guess for the next surface charge density. We repeated this process until we reach the target surface charge density of 0.061 C/m^2 on the walls. For a detailed derivation and numerical implementation of the Langevin-Poisson-EQT method, see Ref. [30].

VI. RESULTS AND DISCUSSION

A. Bulk

As mentioned in Sec. II, we adopt two approaches to obtain the fluid-fluid CG potentials for the extended dipole molecules. The potentials obtained via the charge optimization method are referred to as CGq, and those obtained by the dielectric permittivity optimization are denoted by CGqε. Figure 2 shows the vdW CG potentials and RDF profiles from the CGq and CGqε methods.

As illustrated in Fig. 2(b), both methods are able to match the water RDF from the reference AA simulations. Since we are using the relative entropy method, which is a structure-based CG method, it is guaranteed that upon a finely dis-

TABLE I. Charge, dipole moment, and dielectric permittivity values for SPC/E, CGq, and CGqε water models.

Model	A_c	q (e)	μ (D)	ε_r
CGq	0.3544	0.5046	1.399	21.45
CGqε	0.6555	0.6862	1.903	72.92
SPC/E	1.0	0.8476	2.350	71.89

cretized grid space in the pairwise distances, the CG potential can reproduce the target RDF [33,34]. It is interesting to observe that even though our CG model explicitly considers the electrostatic interactions (through a dipole moment), the CG potentials still exhibit a well-known double-well-type shape similar to what has been observed for single-site spherical water CG models. The double-well-type shape potential has been shown to be important to represent the tetrahedral packing of water [38]. A simple Stockmayer fluid [21] (point dipole + LJ interaction site), which does not have a double-well-type shape potential, may not be able to fully represent the tetrahedral packing of the water molecules [24]. Therefore, it is essential to have a double-well shape potential between the dipoles in order to reproduce the water structure. Table I summarizes the values of A_c, charge, dipole moments, and bulk permittivity for SPC/E, CGq, and CGqε water models. The results show that RE minimization alone cannot reproduce the dielectric permittivity of the SPC/E water model. Despite taking into account the dipolar fluctuations in the CG model, relative entropy minimization fails to reproduce the dielectric permittivity of water. Thus, it is necessary to look at correlation functions, other than the RDF, to investigate why the CGqε method is capable of reproducing the dielectric constant of water. Since the dielectric permittivity is directly related to the electrostatic interactions, we investigate the orientational correlation functions in bulk water. For a system of water molecules, complete information regarding the correlations between the molecules (spatially and orientationally) is given by the molecular pair distribution function $g(1, 2) = g(\boldsymbol{r}_1, \boldsymbol{r}_2, \boldsymbol{\Omega}_1, \boldsymbol{\Omega}_2)$, which depends on the positions ($\boldsymbol{r}$) and angles [$\boldsymbol{\Omega} = (\theta, \phi)$] of molecules 1 and 2 [65] [see Fig. 1(b)]. The orientational part of $g(1, 2)$ can be expanded into an infinite basis set of angular functions using generalized spherical harmonics. However, not all terms in the expansion are necessary to obtain insights into the long-range orientational ordering in water. Since the dipole-dipole interaction is the dominant term in the multipole expansion of the long-ranged part of the molecular pair potential, we restrict our attention to the minimal basis set for dipolar molecules first introduced by Wertheim [66]. Thus, $g(1, 2)$ can be approximated by

$$g(1, 2) \approx g(r)S + 3h_\Delta(r)\Delta(1, 2) + \frac{3}{2}h_D(r)D(1, 2), \quad (36)$$

where $g(r)$ is the radial distribution function, $h_\Delta(r)$ is the dipole-dipole pair correlation function, and $h_D(r)$ represents the angular dependence of the dipole-dipole interaction energy. S, $\Delta(1, 2)$, and $D(1, 2)$ are the basis sets and are

defined as

$$S = 1, \quad (37a)$$

$$\Delta(1, 2) = \hat{\boldsymbol{\mu}}_1 \cdot \hat{\boldsymbol{\mu}}_2, \quad (37b)$$

$$D(1, 2) = 3(\hat{\boldsymbol{\mu}}_1 \cdot \hat{\boldsymbol{r}}_{12})(\hat{\boldsymbol{\mu}}_2 \cdot \hat{\boldsymbol{r}}_{12}) - \hat{\boldsymbol{\mu}}_1 \cdot \hat{\boldsymbol{\mu}}_2, \quad (37c)$$

where $\hat{\boldsymbol{\mu}}$ is the unit vector in the direction of $\boldsymbol{\mu}$ and $\hat{\boldsymbol{r}}_{12}$ is the unit vector in the direction of $\boldsymbol{r}_{12} = \boldsymbol{r}_2 - \boldsymbol{r}_1$. Note that these basis sets are orthogonal but not orthonormal. For more information regarding these basis sets and their properties, see Refs. [65–67].

Using the definition of $\Delta(1, 2)$ given by Eq. (37b), we can calculate $h_\Delta(r)$ from MD simulation as

$$h_\Delta(r) = \frac{1}{N\rho_b}\left\langle\sum_{i=1}^{N}\sum_{j\neq i}^{N}\hat{\boldsymbol{\mu}}_i \cdot \hat{\boldsymbol{\mu}}_j\delta(\boldsymbol{r} - \boldsymbol{r}_{ij})\right\rangle. \quad (38)$$

Furthermore, by looking at the definition of the total dipole moment vector [Eq. (12)], we can write

$$\langle\boldsymbol{M}^2\rangle = \sum_{i=1}^{N}\sum_{j=1}^{N}\langle\boldsymbol{\mu}_i \cdot \boldsymbol{\mu}_j\rangle = N\langle\mu^2\rangle + \langle\mu^2\rangle\sum_{i=1}^{N}\sum_{j\neq i}^{N}\langle\hat{\boldsymbol{\mu}}_i \cdot \hat{\boldsymbol{\mu}}_j\rangle. \quad (39)$$

Using Eqs. (38) and (39), we arrive at

$$\langle\boldsymbol{M}^2\rangle = N\langle\mu^2\rangle\left(1 + \int \rho_b h_\Delta(r)d\boldsymbol{r}\right), \quad (40)$$

where the term in the parentheses is the well-known Kirkwood g factor G_k, which is obtained as the asymptotic value of the r-dependent Kirkwood g factor,

$$G_k(r) = 1 + \int_0^r \rho_b h_\Delta(r)d\boldsymbol{r}. \quad (41)$$

It can be seen that for uncorrelated dipoles, the value of G_k is equal to 1.

Figure 3(a) shows the comparison of dipole-dipole pair correlation function from AAMD, CGq, and CGqε. We observe that h_Δ is longer ranged than the radial distribution function and decays in an oscillatory manner consistent with the recent second-harmonic light scattering experiments [68,69]. This long-range behavior has also been observed by previous studies from molecular dynamic simulations [65,70–73]. From AAMD simulations, we observe that there is a strong short-ranged correlation between dipoles of water molecules in the first solvation shell ($\sim$3 Å). This is due to the fact that the hydrogen bonding imposes a strict restriction on the molecular orientations, thus, adjacent water molecules tend to align via H-bond network [37]. In fact, such a strong positive dipole-dipole correlation can partly explain the high dielectric permittivity of hydrogen-bonded fluids such as water [37,74]. It can be seen that the CGqε method captures this feature to a good extent, whereas the CGq method underestimates the first peak in the dipole-dipole pair correlation function. Interestingly, as we move away from the first peak, the CGq method closely follows the AAMD dipole-dipole pair correlation function. This indicates that at longer distances a dipolar representation of water with the CG potentials obtained from the RE minimization is able to reproduce the dipole-dipole pair correlation function. However, according to the definition
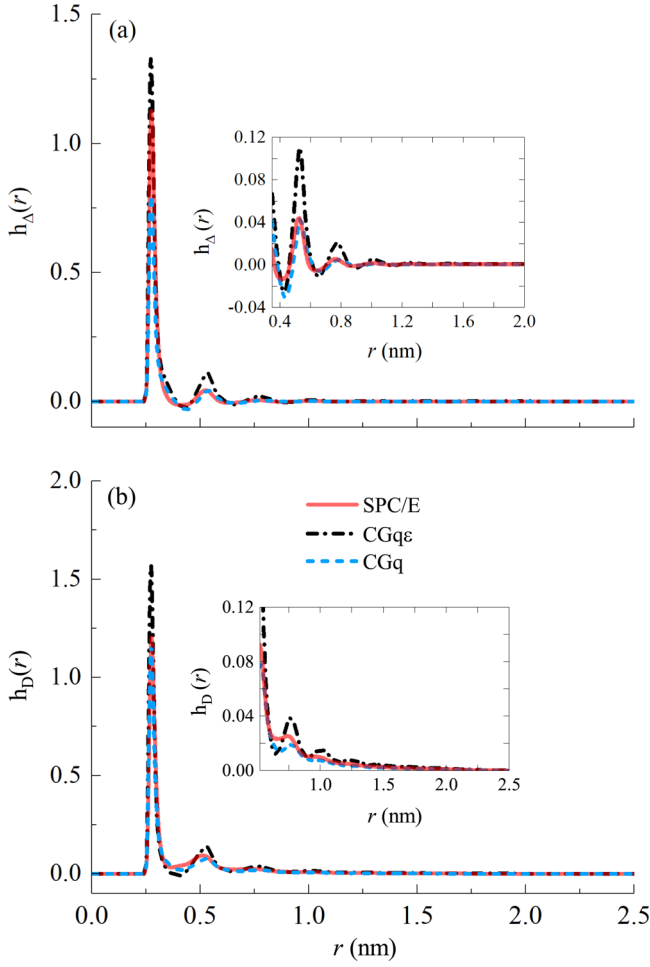
FIG. 3. Orientational correlation functions from AAMD and CGMD simulations: (a) dipole-dipole pair correlation function (b) angular dependent part of the dipole-dipole interaction energy.

FIG. 4. (a) r-dependent Kirkwood factor. (b) The r-dependent local dielectric constant obtained from Eq. (42).

of the bulk permittivity [Eqs. (11) and (40)], we see that the bulk dielectric permittivity depends not only on the G_k (integral of h_Δ) but also on the magnitude of the dipole moment (μ^2). Therefore, solely minimizing the RE function does not guarantee that the water dielectric permittivity is reproduced.

Figure 4(a) shows the r-dependent Kirkwood factor for CG and AA models. It can be seen that $G_k(r)$ asymptotically reaches a plateau. We can also observe that the most important contribution for the SPC/E model comes from the first shell of neighbors, which could be associated with the short-ranged H-bond network in water [37]. It can be seen that the CGqε method follows the SPC/E curve reasonably well up to first coordination shell. Indeed, this is not surprising, as the first peak in the dipole-dipole pair correlation function is better captured by the CGqε method. However, unlike in SPC/E, we observe another jump around 0.6 nm, which causes the curves to deviate from each other. The reason behind this can be understood by looking at locally varying dielectric permittivity, which represents screening variations in the neighborhood of an arbitrary molecule. By using Eqs. (11), (40), and (41), we arrive at

$$\varepsilon_r(r) = 1 + \frac{N\langle\mu^2\rangle G_k(r)}{3\varepsilon_0 V k_B T}. \quad (42)$$
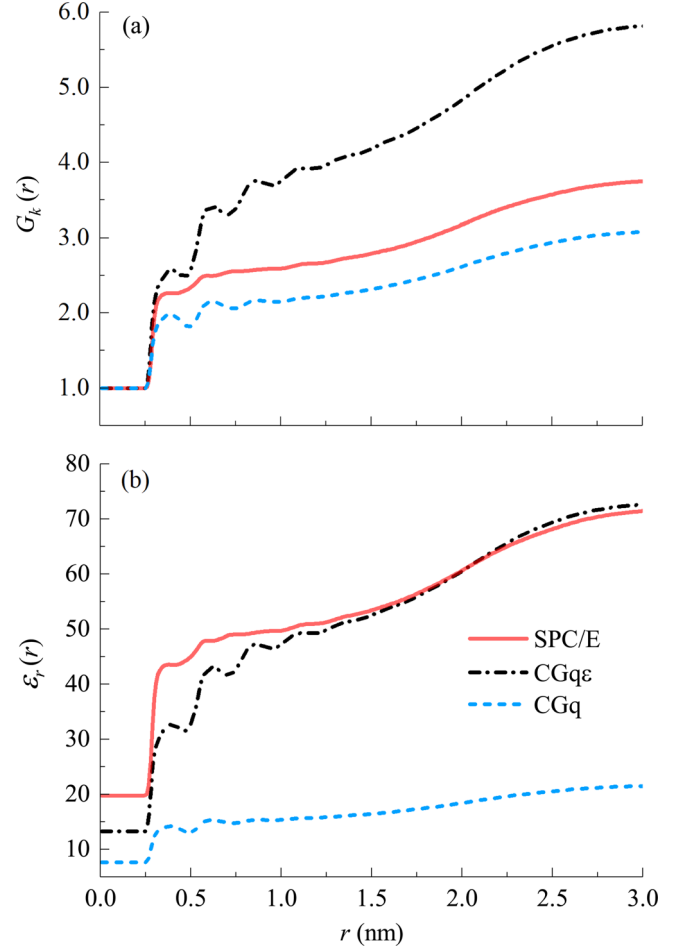
We note that there exist other ways to calculate the local dielectric constant such as using a composite r-dependent Kirkwood factor which combines the results of the constant electric field and constant electric displacement simulations [75].

Figure 4(b) shows the locally varying dielectric permittivity from AA SPC/E model and the CGq and CGqε methods. We observe that the local screening effects are more prominent in the SPC/E model, whereas in the CGqε method these effects are underestimated. Thus, the dipoles are more correlated from the CGqε method compared to the AA SPC/E model [see Figs. 3(a) and 4(a)]. However, by construction, the CGqε is able to converge to the SPC/E model beyond 2.5 nm, where dipoles are not correlated and the value of the permittivity reaches its macroscopic value. On the other hand, although CGq method is able to reproduce the AAMD dipole-dipole pair correlation function reasonably well (especially at longer distances) due to its low dipole moment, it drastically underestimates the screening effects; hence, it fails to reproduce the dielectric constant of water.

Another important quantity that can be studied is $h_D(r)$, which represents the angular dependence of the dipole-dipole

TABLE II. Electrostatic potential energy for SPC/E, CGq, and CGqε water models.

Model	U^{elec} (kJ/mol)	A_c
SPC/E	-121459.02	1.0
CGq	-18848.88	0.3544
CGqε	-42971.05	0.6555
SPC/E (dipole-dipole)	-53175.6	1.0

interaction energy, and can be defined as

$$h_D(r) = \frac{1}{N\rho_b}\left\langle \sum_{i=1}^{N}\sum_{j>i}^{N}[3(\hat{\boldsymbol{\mu}}_i \cdot \hat{\boldsymbol{r}}_{ij})(\hat{\boldsymbol{\mu}}_j \cdot \hat{\boldsymbol{r}}_{ij}) - \hat{\boldsymbol{\mu}}_i \cdot \hat{\boldsymbol{\mu}}_j] \right.$$
$$\left. \times \delta(\boldsymbol{r} - \boldsymbol{r}_{ij}) \right\rangle. \tag{43}$$

Using Eq. (43) we can write the expression between $h_D(r)$ and average electrostatic dipolar energy as follows:

$$\langle U^{dd} \rangle = -4\pi N\rho_b \int_0^\infty \mu^2 \frac{h_D(r)}{r} dr. \tag{44}$$

Note that in Eq. (44) we use the convention $4\pi\varepsilon_0 = 1$ for simplicity. Figure 3(b) shows the comparison of $h_D(r)$ from AAMD, CGq, and CGqε. Unlike $h_\Delta(r)$, the correlation function $h_D(r)$ is almost positive everywhere, suggesting that the preferable alignment of dipoles is to lower the dipole-dipole interaction energy [65]. Moreover, by examining the inset of Fig. 3(b), we observe that $h_D(r)$ is much longer ranged than dipole-dipole pair correlation function, as $h_D(r)$ represents the angular dependent part of the dipole-dipole interaction energy and decays as $\sim r^{-3}$ at large distances. However, the results reported from MD simulations are somewhat inconclusive [71]. Although it seems that the h_D correlation function decays to zero beyond 25 Å, recent large scale MD simulations have shown that it has a nonvanishing tail even at 75 Å [70,76]. However, in order to have a one to one comparison with the experiment and to precisely determine the range at which h_D decays to zero, it requires a very large simulation box (at least 10 nm) [69], which is computationally expensive from AAMD simulations. From the CGMD simulations, it can be seen that the CGq method is able to capture the variation in h_D correlation function to a good extent. This is a promising result which can accelerate the simulations compared to AAMD and provide insights into long-ranged behavior of dipolar alignment with respect to a vector along their separation distance, that can be a subject of future studies. Table II summarizes the total dipole electrostatic energy from AAMD, CGq, and CGqε simulations. As mentioned in Sec. III A, scaling the CGq electrostatic potential by the factor A_c^{-1} recovers the all-atom dipole electrostatic potential. However, Eq. (44) cannot represent the full electrostatic potential of the system of water molecules, as the higher dipole moment of water plays an important role in the electrostatic potential of the system.

Finally, as mentioned in Sec. III C, to match the diffusion coefficient, we optimized the mass of the molecule via simplex algorithm after obtaining the CG potential parameters via the CGqε method. Table III summarizes the results for

TABLE III. Mass and the diffusion coefficient values for the CGqε and SPC/E water models.

Model	m (amu)	D (10^{-5} cm^2/s)
SPC/E	18.0154	2.5875 ± 0.1045
CGqε	18.0154	10.2096 ± 0.0052
CGqε	141.00	2.5606 ± 0.0298

optimal mass and the diffusion coefficient from the downhill simplex algorithm. We observed that optimizing the mass did not affect the structure and the dielectric permittivity value obtained from the CGMD simulations.

B. Confinement

1. Neutral walls

Figure 5 shows the pair potential between carbon and water from all-atom and coarse-grained representation. We observe that upon coarse graining water into extended dipole molecules, the effective wall-fluid pair potential is no longer of the 12-6 LJ interaction form. In fact, the CG optimization yields a double-well-type pair potential, suggesting that the energy and length scales have to be altered in order for the CG model to reproduce water structure at the interface.

Figure 6 shows the density profiles of water inside slitlike graphene channel of width 10σ from both AAMD and CGMD simulations. In this figure, "wflj" refers to the wall-fluid interaction used to perform the confined AAMD simulations (i.e., standard 12-6 LJ interaction between carbon and oxygen). We observe that the confined CG system, in which a water molecule is coarse grained into an uncharged spherically symmetric bead (CG-wflj), overestimates the first density peak and exhibits a shoulder peak at about 2 molecular diameter
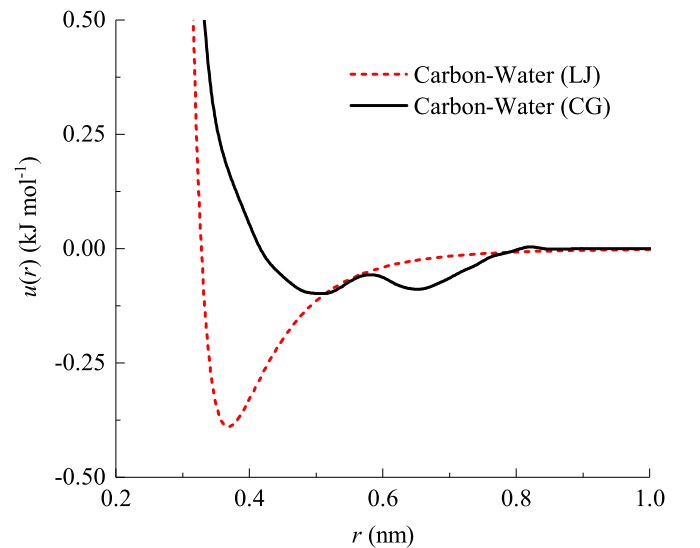

FIG. 5. Carbon-water pair potentials used in AAMD and CGMD simulations. The red color (dashed line) represents the 12-6 LJ potential between carbon and oxygen. The black color (solid line) is the coarse-grained carbon-water interaction obtained by relative entropy minimization.
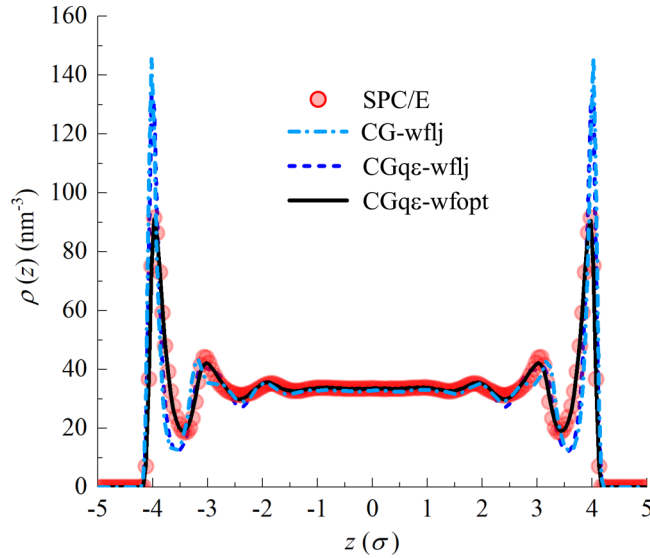
FIG. 6. Comparison of the water density profiles from CGMD and AAMD simulations inside a 10σ channel with different fluid-fluid and wall-fluid pair potentials.

away from the wall compared to the AA SPC/E water model. This clearly shows that the bulk fluid-fluid potential optimized for the single-site CG water is not transferable to the non-bulk (inhomogeneous) environment [24]. In other words, the molecular packing of the water molecules close to an interface is quite different than in bulk. Thus, it is not surprising that an isotropic single-site CG model of water fails to accurately predict the confined water density profile [40,77]. On the other hand, switching from the confined single-site representation to the extended dipole model (CGqε-wflj), improves the water density distribution beyond the first valley (0.5 nm away from the wall), making the model more transferable and shows the role of the anisotropic forces in the fluid-fluid CG potential arising from the explicit electrostatic interactions. However, the density nearby the interface (where the wall-fluid interaction is dominant) is not well captured compared to the AA distribution, which indicates that the LJ wall-fluid interaction is too attractive for the confined CG system. This fact is more evident by looking at Fig. 5, where the energy scales associated with the CG wall-fluid potential are much less than the depth of the carbon-water LJ potential well. Thus, by optimizing the wall-fluid interaction and using the bulk fluid-fluid CG potential for the extended dipole model (CGqε-wfopt), the water structure can be predicted reasonably well when compared to the AAMD simulation. From here on, unless otherwise noted, by CGMD simulation we refer to the confined extended dipole system with the CG wall-fluid potential (CGqε-wfopt).

It is well known that the presence of a solid surface not only gives rise to density variations in the direction perpendicular to the solid surface, but also affects the molecular packing of the fluid parallel to the interface. For this purpose, we have divided the density profile into three regions: (I) interfacial region, (II) intermediate, and (III) bulklike region [see Fig. 7(a)]. In each layer we have calculated the water center-of-mass in-plane (lateral) RDF and compared that to

the bulk radial distribution function. The RDFs are calculated in the slabs centered at the location of the maximum density with a thickness of 1 Å to avoid interference of atoms from the adjacent layers [78]. The in-plane RDF provides information on how molecules arrange in the plane parallel to the wall (here, x-y plane), hence, it can be used to identify ordering and possible phase transition close to an interface [79–81]. A CG model that can capture structural variations both in the parallel and perpendicular directions to an interface can be of high value. Figures 7(b) and 7(c) show the lateral RDFs for regions I and II from both AAMD and CGMD simulations. Compared to the bulk, the radial distribution of the contact layer (region I), is more structured and pronounced, showing a higher degree of ordering in the liquid. It can be seen that the results from the CGMD simulation are in good agreement with that of AAMD simulations. Moving away from the wall, in region II, although we observe that the first valley of the lateral RDF in AAMD is shallower than the bulk RDF, the location of the peaks and valleys follows closely the bulk radial distribution function. This indicates that the in-plane water structure in region II is similar to that of bulk with a slightly higher density. In this region, the CG potentials result in an RDF very similar to that of bulk and in good agreement with AAMD simulation results.

To further test the applicability of our CG potentials, we simulated water in narrower confinements such as 7σ and 4σ channels. Figure 8(a) shows the comparison of the density profiles from AAMD, CGMD, and EQT simulations. Since all the channels are in chemical equilibrium with the same bulk reservoir, the CG potentials are transferable across channels of different width. It can be seen that the results from CGMD simulations are close to AA SPC/E water model. Thus, as far as the structural properties are concerned, the physics nearby the wall is captured well upon optimizing the wall-fluid interaction.

Furthermore, from a continuum perspective, the use of CG potentials together with mean field approximation and FMT functional provides a good description of water molecular arrangement inside the neutral graphene slit channels. It is important to mention that for the neutral wall, the EQT formulation does not explicitly take into account the dipole-dipole interactions, yet we observe that except for a very narrow channel such as 4σ, where it is likely that the fluid-fluid correlations play an important role, the EQT predictions are in good agreement with AAMD and CGMD results.

One of the benefits of using the extended dipole CG model is that it retains the dipolar information necessary for permittivity calculation. This is important, as it can explicitly account for the water screening effects in confinement. For many confined systems where properties vary spatially in the confined direction, the dielectric permittivity has a tensorial form. For a slab geometry, the dielectric constant has two components that vary with the z direction (inhomogeneous axis): parallel [$\varepsilon_{r,\parallel}(z)$] and perpendicular [$\varepsilon_{r,\perp}(z)$] to the wall. To calculate each of the components, we use the fluctuation formulas derived by Ballenegger and Hansen [82]. Figure 8(b) shows the variation of the normalized parallel permittivity for different channel widths. The values are normalized by the bulk AA SPC/E dielectric constant value of 71.89. In the 10σ channel, where both the layered structure and bulk region
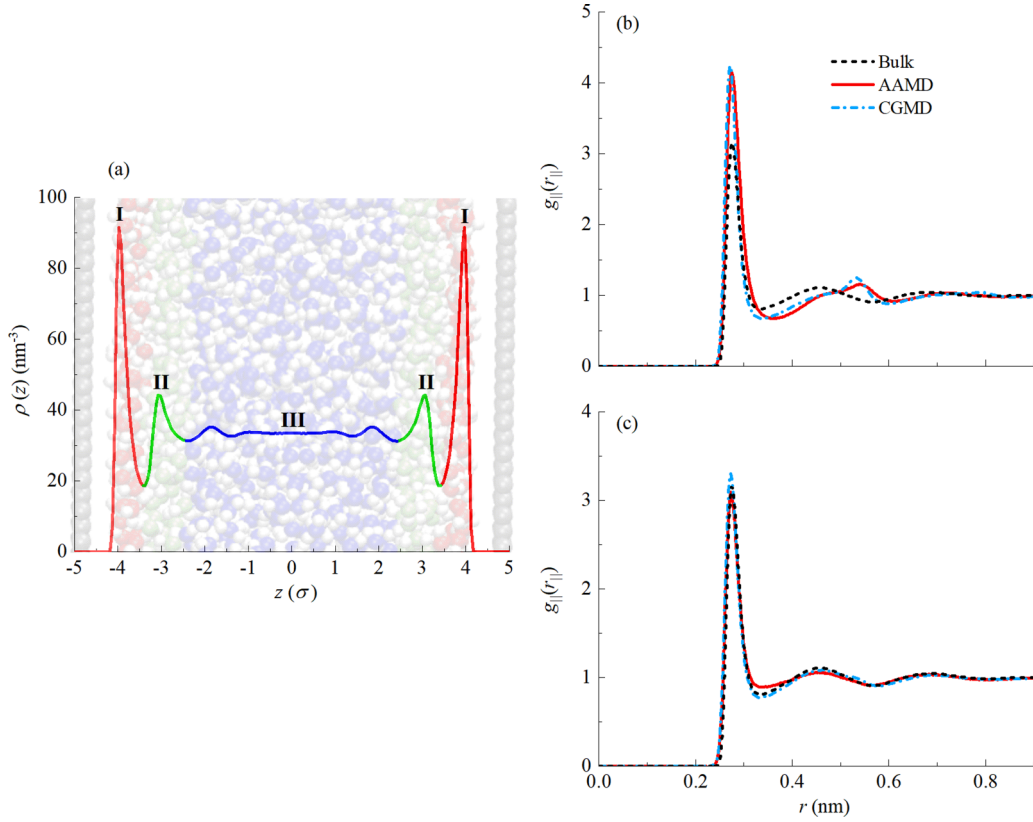
FIG. 7. (a) Snapshot of water confined in a 10σ graphene channel. We define three different regions: an interfacial region (I), an intermediate region (II), and a central region (III), where the in-plane RDF does not show any significant deviation from the bulk RDF. Hydrogen atoms are depicted as white and oxygen atoms are colored as red, green, and blue in regions I, II, and III, respectively. The in-plane RDFs from AAMD and CGMD simulations correspond to regions I (b) and II (c). The dashed line in the figure represents the in-plane RDF far from the surfaces (bulk).

are well formed, the dielectric permittivity is not constant, but it exhibits an oscillatory behavior in an interfacial region of three to four molecular diameters. For such a channel, the water screening strength parallel to the wall is seen to be ∼5 times higher than that of bulk. This emphasizes the need of using a realistic CG model that can capture such pronounced oscillations near an interface. As we move away from the wall, $\varepsilon_{r,\parallel}(z)$ decays until it reaches the bulk value at roughly 4 molecular diameters away from the surface. It can be seen that on average, $\varepsilon_{r,\parallel}$ of water is higher than its bulk value, indicating that the in-plane (xy) screening effects are enhanced by the presence of a planar interface. This is also in agreement with the results of previous studies for planar interfaces [29,83]. It can be seen that except for a very narrow confinement (4σ channel) the extended dipole CG model does a reasonable job in reproducing the parallel component of water dielectric permittivity compared to the AAMD simulations. In the 4σ channel, due to the extreme confinement effect in the z direction, the molecules are closely spaced and packed in the x-y plane, which results in an enhancement of dipole-dipole correlations parallel to the surface [84]. Under these circumstances, we see that the CG model overestimates the parallel dielectric constant. This means that the dipoles are more strongly correlated in the CG representation compared to their AA counterpart. This fact is more evident by looking at the in-plane RDF of the contact layer [see Fig. 7(b)], where

the CG model slightly overestimates the lateral RDF, which can be magnified in the case of extreme confinement such as in the 4σ channel. Furthermore, although optimizing the wall-fluid potential improved the CG density profile significantly, $u_{\mathrm{CG}}^{\mathrm{wf}}$ is isotropic and does not directly take into account the orientational degrees of freedom.

2. Capacitor walls

In this section, we comment on the applicability of the EQT and the CG model on reproducing the density, polarization, and dipolar angle profiles of water inside a capacitorlike channel (negative and positive walls). For this purpose, we simulated water in the presence of an external electric field generated from the negative and positive partial charges on the left and right graphene sheets. We calculated the density, dipolar angle, and polarization profiles from both atomistic and continuum simulations. Due to the presence of the charges on the wall, in addition to the vdW interactions, we have to consider the electrostatic interactions arising from the charge-dipole and dipole-dipole interactions in the EQT framework. For this purpose, we use the EQT-Langevin-Poisson framework, in which the effective electrostatic potential is calculated through the Poisson equation, and the water permittivity and polarization variations are modeled using the LD approximation. Figure 9(a) shows the result for water density profile
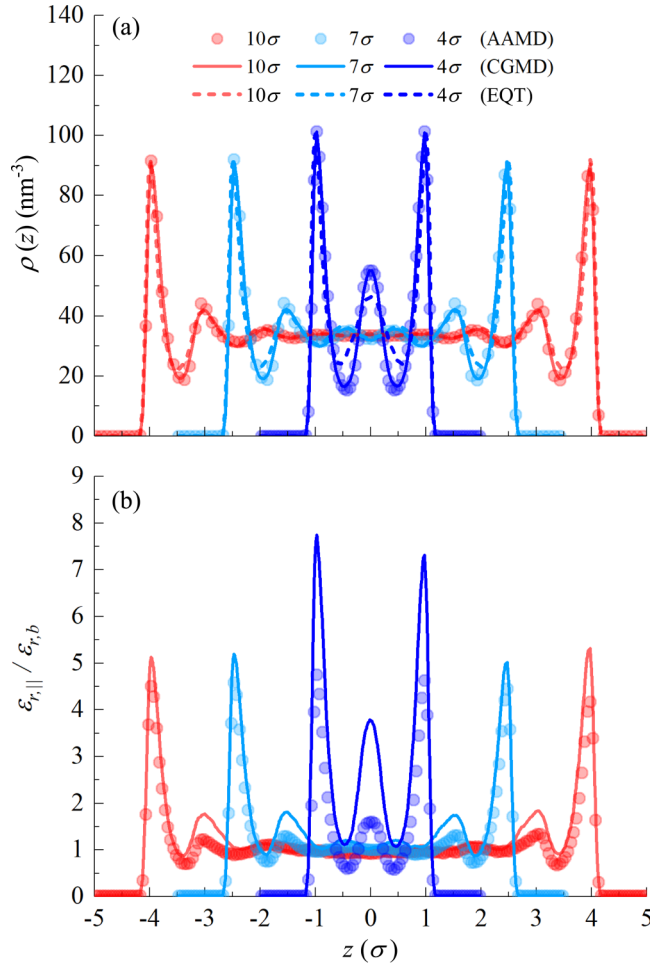
FIG. 8. Water density distributions (a) and parallel permittivity profiles (b) inside graphene slitlike channels of various widths. In the figure, circles, solid line, and dashed line represent AAMD, CGMD, and EQT results, respectively.

FIG. 9. Comparison of water density profile in a capacitor channel of width 12σ.

in the charged 12σ channel from AAMD, CGMD, and EQT simulations. We observe that the AA water density profile is asymmetric with respect to the middle of the channel, and exhibits more pronounced peaks next to the positively charged interface. At the positively charged wall, due to the favorable electrostatic interactions between the wall and water, more oxygen atoms are attracted to the surface creating a region of high density at the interface. This causes the water dipole moments to point away from the wall, making more hydrogens available to form H-bonds with the neighboring water molecules, and resulting in an increase in water density in the preceding layer. As we move towards the middle of the channel, the layering is suppressed and the bulklike region is recovered in the central region of the channel. From the CGMD simulations, the extended dipole model is able to predict the density of water molecules. However, it fails to quantitatively capture the density close to the negatively and positively charged walls. This is expected as, unlike the SPC/E AA water, the extended dipole model is incapable of forming H-bonds, and the CG wall-fluid interaction has been optimized for the neutral walls, which may not be transferable to the charged walls. The former is a limitation of the model,
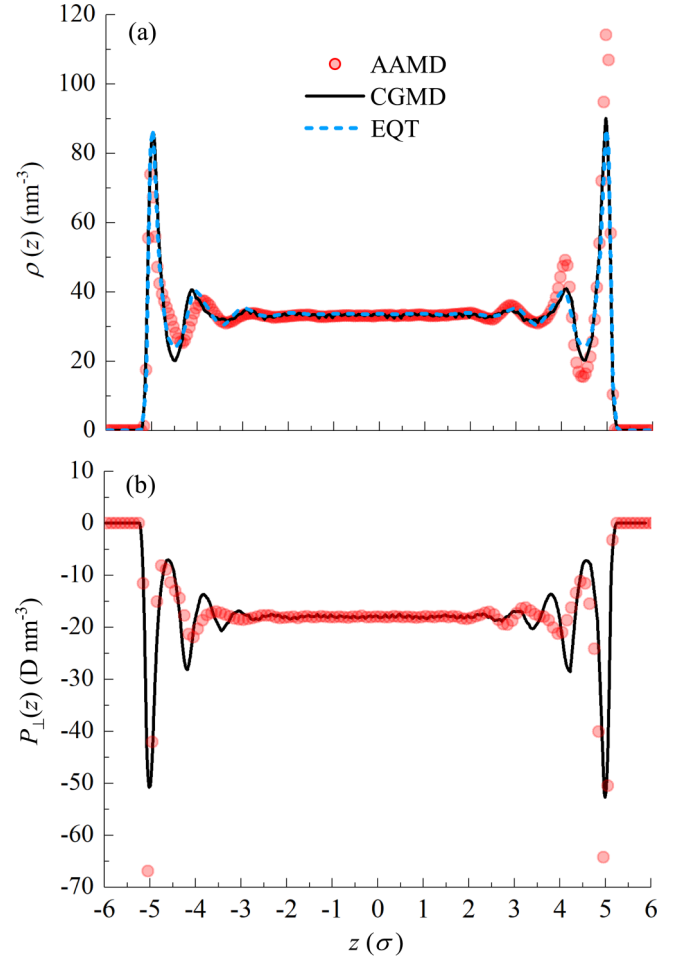
while the latter is the result of the well-known transferability problem of the bottom-up coarse-graining approaches. Nevertheless, the CG model is able to predict the perpendicular polarization $[P_\perp(z)]$ profile in a reasonable agreement with the AAMD simulation [see Fig. 9(b)]. This indicates that to a good extent the perpendicular permittivity variations are being captured, as the $P_\perp(z)$ is proportional to the weak electric field in the cavity by $\varepsilon_{r,\perp}$, according to the linear response theory [29].

The EQT results for density match with the CGMD simulation, which indicates that the hard sphere approximation and the mean field treatment of the electrostatic interactions together with the use of CG potentials, are capable of capturing the structural variations of the dipolar molecules inside the charged confinement. However, by looking at Fig. 10(b), we observe that the EQT-Langevin-Poisson approach cannot capture the variations in the $P_\perp(z)$. Upon a closer inspection, we see that the bulk polarization value is underestimated even though the same dipole moment as CGMD simulations is used. To understand this better, we examine the average cosine of dipole orientation profile since it directly affects the polarization [see Eq. (35)]. Figure 10(a) shows the average orientation profiles from both EQT and CGMD simulations. EQT predicts a higher alignment of dipoles at the charged
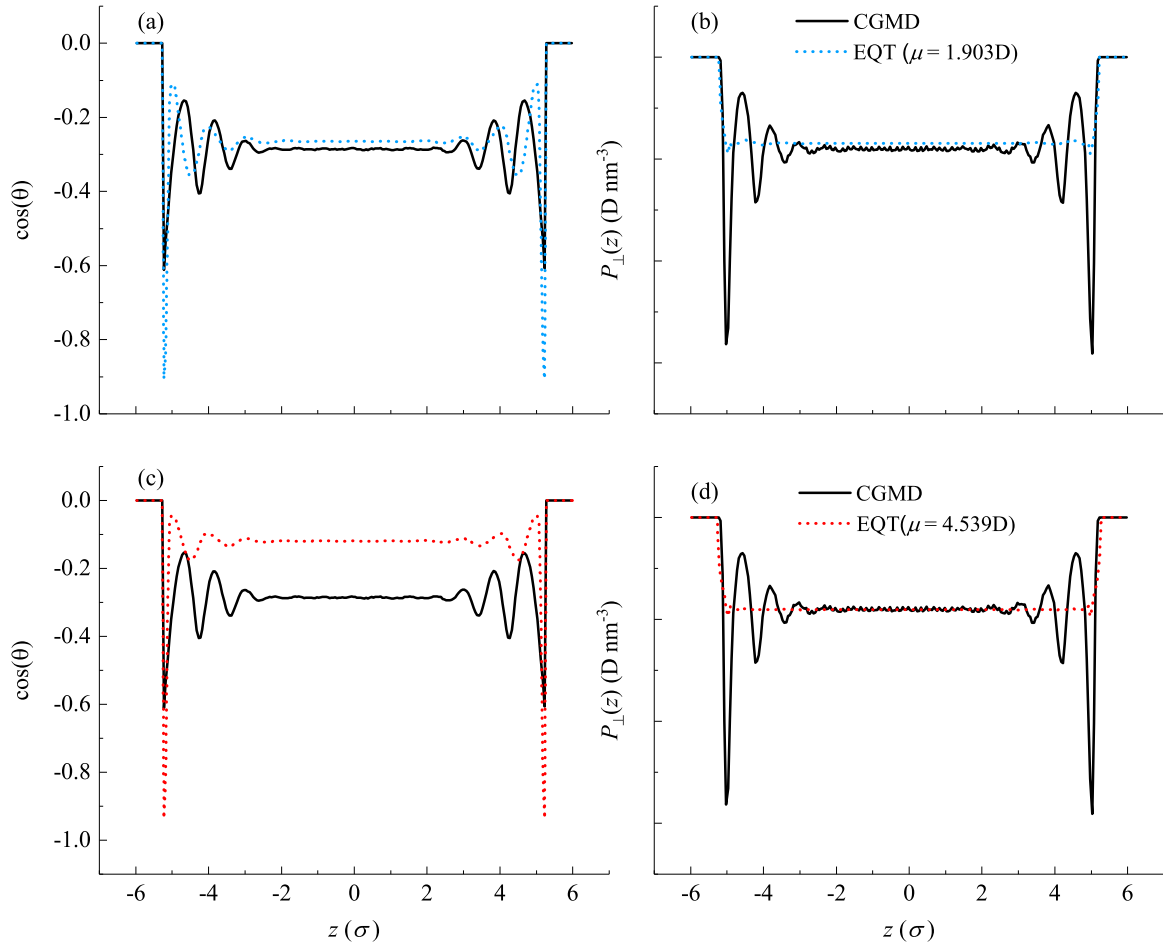
FIG. 10. Water dipolar orientation and polarization profiles from CGMD and EQT simulations inside a capacitor channel of width 12σ.

walls compared to the CGMD simulations, resulting in an overscreening of the external electric field that leads to a lower (in magnitude) dipole orientation in the middle of the channel. Nevertheless, EQT is able to qualitatively capture the oscillations in the average orientation profile with an offset in the location of the peaks and valleys. This is important in computing the perpendicular polarization. Since these structural variations occur over a few nanometers in the vicinity of the interface, even a few angstroms offset in the dipole orientation can drastically affect the polarization profile.

Figure 11 shows the permittivity predicted by the EQT-Langevin-Poisson approach with two different dipole moments. It can be seen that when the CGMD dipole moment of 1.903 D is used, the bulk permittivity is not recovered. Thus, the dipole moment is optimized such that the bulk permittivity is recovered. With a dipole moment of 4.539 D, the polarization of water molecules in the bulk matches that of CGMD simulation [see Fig. 10(d)]. However, the variations are still missing. This can be attributed to two factors: the oversimplifications made in the LD approximation, and the definition of the permittivity used in the theory. In LD approximation, the molecules are treated as noninteracting dipoles, thus the dipole correlations are completely neglected, whereas in the CGMD simulations the dipoles are interacting due to the electrostatic interactions. Furthermore, in the Poisson equation, the dielectric permittivity has been modeled via

one of the following approaches: using a bulk-based relation that is applicable only in the bulk or weakly inhomogeneous
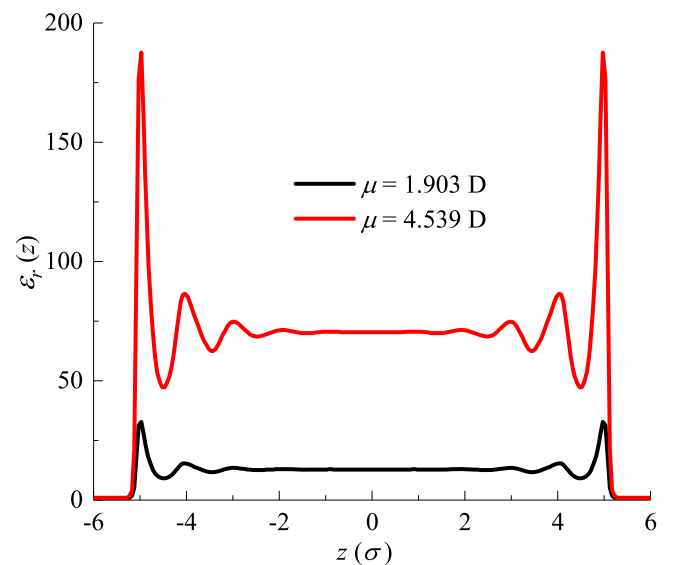

FIG. 11. Dielectric permittivity profiles of water from the Langevin dipole model inside a capacitor channel of width 12σ with different dipole moments.

systems, e.g., Clausius-Mossotti (CM) expression [85], phenomenological formulas that express permittivity in terms of the local density variations [85,86], or a uniform distribution approximation throughout the inhomogeneous system. As mentioned in Sec. VI B 1, for a confined system, however, the dielectric permittivity has a tensorial form. Unlike the parallel permittivity that varies smoothly and locally follows the density oscillations, the perpendicular component exhibits a nonlocal behavior [8] with an average value as small as ~ 2 compared to the bulk [87], suggesting that using bulk-based relations or local density approximations may not be an accurate way of modeling the permittivity in the Poisson equation.

VII. CONCLUSIONS

In this work, we developed an extended CG dipole model for water that reproduces RDF, diffusion coefficient, and dielectric constant at room thermodynamic conditions. We showed that by merely minimizing the RE, one cannot reproduce the dielectric permittivity of bulk water. Thus, we employed the CRE method to optimize the charges and the pair potential such that the dielectric permittivity in the CG system matches that of the SPC/E AA reference simulations. We calculated the dipolar correlations in the bulk system from both CGMD and AAMD simulations. We found that the CGq method is able to capture the AAMD dipole-dipole pair correlation function. However, due to its lower screening and dipole moment, it fails to reproduce the AA SPC/E water dielectric permittivity. On the other hand, the CGqε method results in dipole moment and CG potential that reproduced water dielectric permittivity, although the local screening effects are slightly underestimated compared to that of AA SPC/E model. Furthermore, we matched the diffusion coefficient by systematically optimizing the mass of the molecule via simplex algorithm. To test our model, we demonstrated it by simulating water in slitlike graphene nanochannels of various widths. We observed that without any modification to the wall-fluid interactions, the density profiles were in a good agreement with the AAMD simulations, emphasizing the role of anisotropic forces arising from the inclusion of the electrostatic interactions in the CG model. In order to obtain a quantitative agreement, we coarse grained the wall-water interaction. Our results, revealed that the nature of the CG wall-water interaction is no longer of the 12-6 LJ potential form, but a double-well-type potential with a lower attractive potential well. We showed that the agreement in density profiles from AAMD, CGMD, and EQT is good. We further calculated properties such as in-plane RDFs, and parallel dielectric permittivity, and showed that the CG model is capable of reproducing these quantities in a good agreement with the AAMD simulations. Finally, to test the applicability of our

model in screening the charges perpendicular to an interface, we simulated water in a capacitor wall and calculated the density, dipolar angle, and polarization profiles. Ignoring the dipole-dipole interactions (LD approximation) and improper modeling of the perpendicular permittivity in the Poisson equation fails to capture the variations in the polarization profile, thereby providing an inaccurate picture of charge screening in confinement. However, due to the presence of dipoles and systematic parametrization, our CG model captures the polarization profile observed in AAMD simulations, suggesting that the water screening effects perpendicular to the wall have been captured to a good extent. We note that the method developed in this paper is not limited to water and can be used to coarse grain other polar molecules.

APPENDIX: DERIVATIVE OF DIELECTRIC PERMITTIVITY WITH RESPECT TO A_c

For a bulk system with periodic boundary condition, the dielectric permittivity can be calculated as

$$\varepsilon_r = 1 + \frac{\langle \boldsymbol{M}^2 \rangle}{3\varepsilon_0 V k_B T}, \qquad (A1)$$

where the total dipole moment squared can be expressed in terms of the Kirkwood correlation factor G_k:

$$\langle \boldsymbol{M}^2 \rangle = N\mu^2 G_k. \qquad (A2)$$

In the CG model, we scale the all-atom charges via a factor A_c. Thus, using Eq. (A2), the total dipole moment square for the CG system can be written as

$$\langle \boldsymbol{M}^2 \rangle = N A_c q^2 G_k. \qquad (A3)$$

Hence, the derivative of the dielectric permittivity with respect to A_c can be written as

$$\frac{\varepsilon_r}{A_c} = \frac{N q^2 G_k}{3\varepsilon_0 V k_B T}. \qquad (A4)$$

Using Eqs. (A1), (A3), and (A4), we arrive at

$$\frac{d\varepsilon_{r,\mathrm{CG}}}{dA_c} = \frac{\varepsilon_{r,\mathrm{CG}} - 1}{A_c}. \qquad (A5)$$

[1] J. Israelachvili and H. Wennerström, Nature (London) **379**, 219 (1996).

[2] D. J. Bonthuis, S. Gekle, and R. R. Netz, Langmuir **28**, 7679 (2012).

[3] M. A. Shannon, P. W. Bohn, M. Elimelech, and J. G. Georgiadis, Nature (London) **452**, 301 (2008).

[4] M. Heiranian, A. B. Farimani, and N. R. Aluru, Nat. Commun. **6**, 8616 (2015).

[5] K. A. Dill, Biochemistry **29**, 7133 (1990).

[6] M.-C. Bellissent-Funel, A. Hassanali, M. Havenith, R. Henchman, P. Pohl, F. Sterpone, D. van der Spoel, Y. Xu, and A. E. Garcia, Chem. Rev. **116**, 7673 (2016).

[7] A. Ben-Naim, *Molecular Theory of Water and Aqueous Solutions: The Role of Water in Protein Folding, Self-assembly and Molecular Recognition* (World Scientific, Singapore, 2011), Vol. 2.

[8] D. J. Bonthuis, S. Gekle, and R. R. Netz, Phys. Rev. Lett. **107**, 166102 (2011).

[9] M. Armand, F. Endres, D. R. MacFarlane, H. Ohno, and B. Scrosati, *Materials For Sustainable Energy: A Collection of Peer-Reviewed Research and Review Articles from Nature Publishing Group* (World Scientific, Singapore, 2011), pp. 129–137.

[10] K. Graf, M. Kappl *et al.*, *Physics and Chemistry of Interfaces* (Wiley, Hoboken, NJ, 2006).

[11] R. Qiao and N. Aluru, J. Chem. Phys. **118**, 4692 (2003).

[12] R. Qiao and N. R. Aluru, Phys. Rev. Lett. **92**, 198301 (2004).

[13] K. M. Salerno, A. L. Frischknecht, and M. J. Stevens, J. Phys. Chem. B **120**, 5927 (2016).

[14] H. A. Stern and S. E. Feller, J. Chem. Phys. **118**, 3401 (2003).

[15] C. Schaaf and S. Gekle, J. Chem. Phys. **145**, 084901 (2016).

[16] Y. Liu and T. Ichiye, J. Phys. Chem. **100**, 2723 (1996).

[17] P. Teixeira, J. Tavares, and M. T. da Gama, J. Phys.: Condens. Matter **12**, R411 (2000).

[18] V. A. Froltsov and S. H. Klapp, J. Chem. Phys. **124**, 134701 (2006).

[19] G. Raabe and R. J. Sadus, J. Chem. Phys. **134**, 234501 (2011).

[20] S. Riniker and W. F. van Gunsteren, J. Chem. Phys. **134**, 084110 (2011).

[21] W. H. Stockmayer, J. Chem. Phys. **9**, 398 (1941).

[22] D. Bratko, L. Blum, and A. Luzar, J. Chem. Phys. **83**, 6367 (1985).

[23] E. Ávalos, F. del Río, and S. Lago, J. Phys. Chem. B **109**, 508 (2005).

[24] T. Rodríguez-López, Y. Khalak, and M. Karttunen, J. Chem. Phys. **147**, 134108 (2017).

[25] M. Orsi and J. W. Essex, PLoS One **6**, e28637 (2011).

[26] M. Orsi, Mol. Phys. **112**, 1566 (2014).

[27] P. G. Lafond and S. Izvekov, J. Chem. Theory Comput. **12**, 5737 (2016).

[28] A. Moradzadeh, M. H. Motevaselian, S. Y. Mashayak, and N. R. Aluru, J. Chem. Theory Comput. **14**, 3252 (2018).

[29] V. Ballenegger and J.-P. Hansen, Mol. Phys. **102**, 599 (2004).

[30] S. Mashayak and N. Aluru, J. Chem. Phys. **146**, 044108 (2017).

[31] D. Reith, M. Pütz, and F. Müller-Plathe, J. Comput. Chem. **24**, 1624 (2003).

[32] A. P. Lyubartsev and A. Laaksonen, Phys. Rev. E **52**, 3730 (1995).

[33] M. S. Shell, J. Chem. Phys. **129**, 144108 (2008).

[34] A. Chaimovich and M. S. Shell, J. Chem. Phys. **134**, 094112 (2011).

[35] S. Mashayak, M. N. Jochum, K. Koschke, N. Aluru, V. Rühle, and C. Junghans, PLoS one **10**, e0131754 (2015).

[36] M. Neumann, Mol. Phys. **50**, 841 (1983).

[37] M. Sharma, R. Resta, and R. Car, Phys. Rev. Lett. **98**, 247401 (2007).

[38] H. Wang, C. Junghans, and K. Kremer, Eur. Phys. J. E **28**, 221 (2009).

[39] C.-C. Fu, P. M. Kulkarni, M. S. Shell, and L. G. Leal, J. Chem. Phys. **139**, 094107 (2013).

[40] S. Mashayak and N. Aluru, J. Chem. Theory Comput. **8**, 1828 (2012).

[41] S. Mashayak and N. Aluru, J. Chem. Phys. **137**, 214707 (2012).

[42] T. Sanyal and M. S. Shell, J. Chem. Phys. **145**, 034109 (2016).

[43] J. W. Wagner, T. Dannenhoffer-Lafage, J. Jin, and G. A. Voth, J. Chem. Phys. **147**, 044113 (2017).

[44] S. Izvekov and G. A. Voth, J. Phys. Chem. B **109**, 2469 (2005).

[45] S. Izvekov and G. A. Voth, J. Chem. Phys. **123**, 134105 (2005).

[46] A. Raghunathan, J. Park, and N. Aluru, J. Chem. Phys. **127**, 174701 (2007).

[47] T. Sanghi and N. Aluru, J. Chem. Phys. **132**, 044703 (2010).

[48] T. Sanghi and N. Aluru, J. Chem. Phys. **136**, 024102 (2012).

[49] S. Mashayak and N. Aluru, J. Chem. Phys. **148**, 214102 (2018).

[50] S. Mashayak, M. Motevaselian, and N. Aluru, J. Chem. Phys. **142**, 244116 (2015).

[51] M. Motevaselian, S. Mashayak, and N. Aluru, J. Chem. Phys. **143**, 124106 (2015).

[52] M. Motevaselian and N. Aluru, J. Chem. Phys. **146**, 154102 (2017).

[53] Y. Rosenfeld, Phys. Rev. Lett. **63**, 980 (1989).

[54] Y.-X. Yu and J. Wu, J. Chem. Phys. **117**, 10156 (2002).

[55] R. Roth, R. Evans, A. Lang, and G. Kahl, J. Phys.: Condens. Matter **14**, 12063 (2002).

[56] H. Hansen-Goos and R. Roth, J. Phys.: Condens. Matter **18**, 8413 (2006).

[57] R. Roth, J. Phys.: Condens. Matter **22**, 063102 (2010).

[58] A. Oleksy and J.-P. Hansen, J. Chem. Phys. **132**, 204702 (2010).

[59] M. J. Abraham, T. Murtola, R. Schulz, S. Páll, J. C. Smith, B. Hess, and E. Lindahl, SoftwareX **1**, 19 (2015).

[60] S. Nosé, J. Chem. Phys. **81**, 511 (1984).

[61] J.-P. Ryckaert, G. Ciccotti, and H. J. Berendsen, J. Comput. Phys. **23**, 327 (1977).

[62] A. A. Chialvo and P. T. Cummings, Adv. Chem. Phys. **109**, 115 (1999).

[63] T. Darden, D. York, and L. Pedersen, J. Chem. Phys. **98**, 10089 (1993).

[64] Please see https://github.com/Hosseinmote/Extended-Dipole-Model-for-Polar-Liquids.

[65] G. Mathias and P. Tavan, J. Chem. Phys. **120**, 4393 (2004).

[66] M. Wertheim, J. Chem. Phys. **55**, 4291 (1971).

[67] J.-P. Hansen and I. R. McDonald, *Theory of Simple Liquids* (Elsevier, Amsterdam, 1990).

[68] D. P. Shelton, J. Chem. Phys. **136**, 044503 (2012).

[69] D. P. Shelton, J. Chem. Phys. **141**, 224506 (2014).

[70] J. M. P. Kanth, S. Vemparala, and R. Anishetty, Phys. Rev. E **81**, 021201 (2010).

[71] Y. Liu and J. Wu, J. Chem. Phys. **139**, 041103 (2013).

[72] C. Zhang and G. Galli, J. Chem. Phys. **141**, 084504 (2014).

[73] Q. A. Besford, A. J. Christofferson, M. Liu, and I. Yarovsky, J. Chem. Phys. **147**, 194503 (2017).

[74] S. Goldman and C. Joslin, J. Phys. Chem. **97**, 12349 (1993).

[75] C. Zhang, J. Hutter, and M. Sprik, J. Phys. Chem. Lett. **7**, 2696 (2016).

[76] U. Baul, J. M. P. Kanth, R. Anishetty, and S. Vemparala, J. Chem. Phys. **144**, 104502 (2016).

[77] A. Malani, K. Ayappa, and S. Murad, J. Phys. Chem. B **113**, 13825 (2009).

[78] D. Argyris, N. R. Tummala, A. Striolo, and D. R. Cole, J. Phys. Chem. C **112**, 13587 (2008).

[79] S. Han, M. Choi, P. Kumar, and H. E. Stanley, Nat. Phys. **6**, 685 (2010).

[80] L. B. Krott and M. C. Barbosa, J. Chem. Phys. **138**, 084505 (2013).

[81] A. Barati Farimani and N. R. Aluru, J. Phys. Chem. C **120**, 23763 (2016).

[82] V. Ballenegger and J.-P. Hansen, J. Chem. Phys. **122**, 114711 (2005).

[83] C. Zhang, F. Gygi, and G. Galli, J. Phys. Chem. Lett. **4**, 2477 (2013).

[84] R. Renou, A. Szymczyk, G. Maurin, P. Malfreyt, and A. Ghoufi, J. Chem. Phys. **142**, 184706 (2015).

[85] A. Oleksy and J.-P. Hansen, Mol. Phys. **107**, 2609 (2009).

[86] V. Warshavsky and M. Marucho, Phys. Rev. E **93**, 042607 (2016).

[87] L. Fumagalli, A. Esfandiar, R. Fabregas, S. Hu, P. Ares, A. Janardanan, Q. Yang, B. Radha, T. Taniguchi, K. Watanabe, G. Gomila, K. S. Novoselov, and A. K. Geim, Science **360**, 1339 (2018).